The Astrophysical Journal Letters, 979:L43 (9pp), 2025 February 1 https://doi.org/10.3847/2041-8213/ada9e4

© 2025. The Author(s). Published by the American Astronomical Society.
OPEN ACCESS

High-resolution Observations of an X-1.0 White-light Flare with Moving Flare Ribbons

Xu Yang[1], Meiqi Wang[2], Andrew Cao[3], Kaifan Ji[4], Vasyl Yurchyshyn[1], Jiong Qiu[5], Sijie Yu[2],
Jinhua Shen[6], and Wenda Cao[1,2]
[1] Big Bear Solar Observatory, 40386 N Shore Ln., Big Bear, CA 92314, USA; Xu.Yang@njit.edu, wenda.cao@njit.edu
[2] Center for Solar-Terrestrial Research, New Jersey Institute of Technology, 323 Martin Luther King Jr Blvd., Newark, NJ 07102-1982, USA
[3] Union County Vocational-Technical Schools, 1776 Raritan Rd., Scotch Plains, NJ 07076, USA
[4] Yunnan Observatories, Chinese Academy of Sciences, 396 Yangfangwang, Kunming, Yunnan 650011, People's Republic of China
[5] Department of Physics, Montana State University, Bozeman, MT 59717, USA
[6] Xinjiang Astronomical Observatory, Chinese Academy of Sciences, 150 Science 1-Street, Urumqi, Xinjiang 830011, People's Republic of China

Received 2024 November 6; revised 2024 December 23; accepted 2025 January 12; published 2025 January 29

Abstract

We analyze high-resolution observations of an X-1.0 white-light flare, triggered by a filament eruption, on 2022 October 2. The full process of filament formation and subsequent eruption was captured in the Hα passband by the Visible Imaging Spectrograph (VIS) on board the Goode Solar Telescope (GST) within its center field of view. White-light emissions appear in flare ribbons following the filament eruption and Hα ribbon brightening. GST Broadband Filter Imager data show that the continuum intensity, as compared to the nearby quiet-Sun area, has increased by up to 20% in the photospheric TiO band around 7057 Å. The Helioseismic and Magnetic Imager on board the Solar Dynamics Observatory reported 10% contrast enhancement in the continuum near Fe I 6173 Å line. The separation motion of two white-light kernels is recorded by the high-cadence GST/TiO images and is well accompanied by the motion of the VIS Hα flare ribbon leading edge. One kernel, located in a 150 Gauss field within a granulation area, exhibited an average apparent motion speed of 55 km s^{-1}, which is the highest average speed ever reported. The other kernel drifted at 9 km s^{-1} in an 800 Gauss magnetic field area. Hard X-ray (HXR) emissions reaching up to 300 keV have been observed for this flare. The simultaneous occurrence of high-cadence HXR, microwave, and white-light emissions strongly suggests that the energetic particles from the flare directly contribute to the heating. The inverted HXR energy flux density corresponding to 10% TiO brightening is $2.07 \pm 0.23 \times 10^{11}$ erg cm^{-2} s^{-1} during the flare peak.

Unified Astronomy Thesaurus concepts: Solar white-light flares (1983); Solar filament eruptions (1981); Solar photosphere (1518); Solar chromosphere (1479)

Materials only available in the online version of record: animations

1. Introduction

White-light flares (WLFs) have been observed in the near-ultraviolet continuum (P. Heinzel & L. Kleint 2014), visible (e.g., D. Neidig 1989), and near-infrared continuum (e.g., Y. Xu et al. 2004, 2006) ranges of the solar spectrum for several decades. Recent studies based on data from the Advanced Space-based Solar Observatory (ASO-S; W. Gan et al. 2023) focused on WLFs using a short wavelength band at 3600 Å. Although there is no compelling reason why white-light (WL) emission should not be observed in all solar flares (S. A. Matthews et al. 2003; D. B. Jess et al. 2008), high-resolution observations show that some small and moderate flares (GOES X-ray class C and M) may not be associated with any detectable signatures in the TiO red-continuum data (V. Yurchyshyn et al. 2017). N.-Y. Huang et al. (2016) studied 25 flares of GOES X-ray class M5.0 and above and detected 13 WLFs using continuum intensity (I_c) data from the Helioseismic and Magnetic Imager (HMI; J. Schou et al. 2011) on board the Solar Dynamics Observatory (SDO; P. H. Scherrer et al. 2011). K. Watanabe et al. (2017) statistically studied 101 GOES M- and X-class flares observed using the Hinode Solar Optical Telescope (SOT; Y. Suematsu et al. 2008) and SDO/HMI visible continuum, and identified 49 WLFs and 52 non-WLFs. Z. Jing et al. (2024) analyzed 205 flares observed by the ASO-S stronger than the M1.0 class and identified 49 WLFs at 3600 Å.

WLFs are classified into two different types (M. E. Machado et al. 1989). Type I WL emission is temporally and spatially well related to nonthermal electrons produced in flares (H. S. Hudson et al. 1992; T. R. Metcalf et al. 2003; N.-Y. Huang et al. 2016; M. Kuhar et al. 2016; K. Watanabe et al. 2017; V. Yurchyshyn et al. 2017; Y. Li et al. 2024), while type II WLFs display the absence of such correlations with hard X-ray (HXR), microwave emission, and the Balmer jump in the continuum spectrum (M. D. Ding et al. 1999; O. Procházka et al. 2018). Some studies suggest that WL emission may be associated with flare energetic electrons with energies above 50 keV (e.g., M. Kuhar et al. 2016; V. Yurchyshyn et al. 2017). Harder HXR spectra with a smaller power-law index, indicating an enhanced number of high-energy electrons, may (N.-Y. Huang et al. 2016) or may not (K. Watanabe et al. 2017) contribute to the WL emission.

The fundamental enigma surrounding the formation height of WL emission and its corresponding generation mechanism persists as an unresolved challenge within the scientific community. Several heating mechanisms have been proposed to explain the WL emission, including electron beam bombardment (H. S. Hudson 1972; J. Aboudarham & J. C. Henoux 1986), Alfvén wave dissipation (L. Fletcher & H. S. Hudson

Original content from this work may be used under the terms of the Creative Commons Attribution 4.0 licence. Any further distribution of this work must maintain attribution to the author(s) and the title of the work, journal citation and DOI.

2008), backwarming (M. E. Machado et al. 1989; T. R. Metcalf et al. 1990; P. Heinzel & L. Kleint 2014), and chromospheric condensation (W. Q. Gan & P. J. D. Mauas 1994; A. F. Kowalski et al. 2015). Q. Hao et al. (2012), Y. Song & H. Tian (2018), and Y. Song et al. (2020) reported that WLFs are powered by magnetic reconnection in the lower atmosphere. Based on single-loop Fokker–Planck and radiative hydrodynamics RADYN+FP simulations, V. M. Sadykov et al. (2023) suggested that flare-accelerated protons can also contribute to the heating of the lower atmosphere and the WL emission.

In this study, we present observations of a GOES X1.0-class WL flare displaying distinctive separation motion of WL ribbons. Section 2 introduces the instruments, observations, and data analysis. Section 3.1 describes the formation and eruption of the filament accompanied by the flare. Section 3.2 presents the evolution of the WLF ribbons. Section 3.3 investigates the heating mechanism responsible for WL emission.

2. Observation and Data Reduction

On 2022 October 2, a GOES X1.0 flare occurred in NOAA AR 13110 (691″, 213″, $\mu \equiv \cos\theta = 0.66$) and was observed using the Goode Solar Telescope (GST; P. R. Goode & W. Cao 2012), SDO, Fermi Gamma-ray Space Telescope (Fermi; W. B. Atwood et al. 2009), and Chinese Hα Solar Explorer (CHASE; C. Li et al. 2022). The active region (AR) was observed by GST from 16:10 UT to 22:30 UT, and this study uses data acquired between 18:30 UT and 20:50 UT. An eruption of an Hα filament and post-eruption arcade in the solar chromosphere were recorded by the Visible Imaging Spectrometer (VIS/GST; W. Cao et al. 2010b, 2010a), and the WLF ribbons were recorded by the Broadband Filter Imager (BFI/GST; W. Cao et al. 2010b) and the Near Infrared Imaging Spectropolarimeter on board the GST (NIRIS; W. Cao et al. 2012; K. Ahn et al. 2016).

BFI collects photospheric imaging data using an interference filter with a 10 Å bandpass centered at the TiO 7057 Å molecular band. The resulting images have a scale of 0.″03 pixel^{-1} and a 60″× 60″ field of view (FOV) with a 15 s cadence. The number density of TiO molecules is sufficiently high only inside the sunspot umbra, and it generates higher opacity during the flare (S. V. Berdyugina et al. 2003). The BFI/TiO images are more sensitive than the HMI/I_c to the flare WL emission.

VIS is based on a single Fabry–Pérot etalon that produces a narrow 0.08 Å bandpass over a 74″× 68″ circular FOV. This tunable filter operates within the 5500 ~ 7000 Å range, and the image scale is 0.″029 pixel^{-1} at the Hα 6563 Å line. Images can be acquired at any of the 13 predefined spectroscopic positions (0.2 Å step) centered at the Hα 6563 Å line. Seven wavelengths, including the line center, ±0.4, ±0.6, and ±0.8 Å data, were acquired during the observation period.

The telescopes adaptive optics system (AO-308) utilizes a wave front sensor with 308 subapertures across the telescope pupil. Photospheric TiO images and chromospheric Hα images are speckle reconstructed to further minimize residual aberrations using the KISIP7 code (Kiepenheuer Institute Speckle Interferometry Package; F. Wöger & O. von der Lühe 2007).

NIRIS uses a dual Fabry–Pérot etalon that provides 60″ square FOV full Stokes imaging polarimetry. In our study, NIRIS performed imaging spectropolarimetric observations using the Fe I line at 1.56 μm with an image scale of 0.″08 pixel^{-1}. A total of 40 wavelength positions are scanned, ranging from the line center to ±3.16 Å. The temporal cadence was 26 s for VIS and 51 s for NIRIS during the quiet period. When the flare started, their cadences were decreased to 13.5 s and 31 s, respectively.

The Fermi provides HXR data in the energy range of 25–300 keV with its Gamma-ray Burst Monitor (GBM; C. Meegan et al. 2009). The Expanded Owens Valley Solar Array (EOVSA; D. E. Gary et al. 2018) collects radio imaging spectroscopic data over the 1 ~ 18 GHz frequency range, covering the entire spectrum in 1 s. The Atmospheric Imaging Assembly (AIA) suite of instrumentation (J. R. Lemen et al. 2011) on board the SDO provides us with ultraviolet and extreme-ultraviolet (EUV) images of the solar coronal. The photospheric intensity (I_c) images and the line-of-sight magnetic field measurements ($B_{\rm los}$) were provided by the HMI/SDO instrument.

Data sets of different wavelengths were spatially coaligned to the start time of 18:30 UT by taking the HMI/SDO full-disk continuum intensity image as a reference. The time series of images in each data set are then aligned to that moment. Image registration and coalignment follow the algorithm described in X. Yang et al. (2022). The EUV images from the AIA were carefully aligned (in temporal and spectroscopic dimensions) to a subpixel level accuracy by the Optical Flow algorithm developed by Y.-F. Cai et al. (2022) and X. Yang et al. (2022).

3. Results

Prior to the X1.0 flare, AR 13110 produced a C7.8 flare with a lesser filament eruption at 17:53 UT. The X1.0 flare, accompanied by a much larger filament eruption, began at 19:53 UT according to GOES soft X-ray data. It was a slow-rise flare and the Fermi/GBM HXR flux peaked at 20:22 UT, while the GOES soft X-ray flux peaked at 20:25 UT. GST collected a comprehensive high-resolution imaging data set detailing the emergence of a twisted flux rope, the development and eruption of the filament, as well as the evolution of the flare ribbons and the post-eruption flare loops.

Figure 1 provides an overview of this event. In the early stage of the flare, following the filament eruption, bright ribbons were present along the polarity inversion line (PIL) in EUV and Hα images. Radio observation from EVOSA detected three isolated sources at high frequencies (above 15.8 GHz) that overlapped with the flare ribbons, indicating that energetic particles precipitate at the flare ribbons.

Three WL kernels can be detected in photospheric BFI/TiO and HMI/I_c images during the peak of the flare emission. BFI/TiO reported as high as 20% enhanced intensity to the quiet Sun and HMI/I_c recorded 10%. Three regions of interest (ROIs), K1, K2, and K3 outlined by the black dashed squares, correspond to the flare ribbons and WL kernels. Differential images are made to better present the WL kernel emissions in Figures 3 and 4. An animation corresponding to Figure 3 is available to display the motion of the WLF ribbons. Imaging spectroscopic radio data can be a diagnostic tool to analyze the structure of flare loops. Nonthermal electrons, which gyrate within the coronal magnetic field and generate gyrosynchrotron radiation in the microwave range, can fill the magnetic flux tube. From the line of sight (LOS) near the limb, the projection effect resulting from differing source heights causes a slight displacement of the red contour representing the TiO intensity from the blue contour of the radio source; thus, the ROI K2r

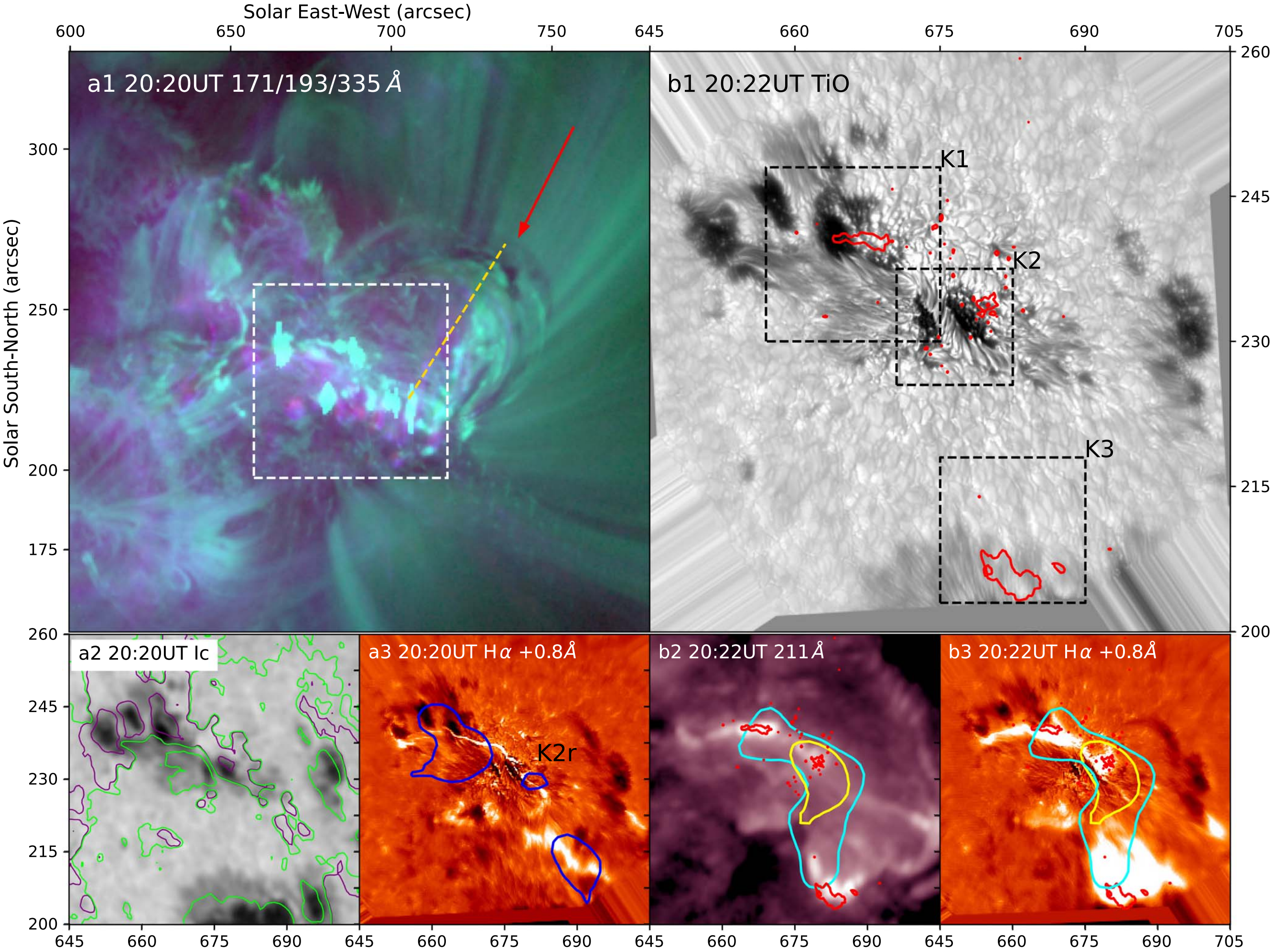

Figure 1. An overview of the filament eruption and the flare. Panel (a1) is composed of AIA 171/193/335 Å images encompassing a large area covering NOAA AR 13110. The red arrow indicates the erupting filament. A white dashed square marks the GST FOV (AR 13110). Panel (a2) shows HMI/I_c image of the same FOV. Green and purple contours represent HMI positive and negative line-of-sight (LOS) magnetic fields. GST Hα red-wing 0.8 Å image in panel (a3) shows the initial location of flare ribbons. Three footpoint resources, resolved by the EOVSA high-frequency imaging data (blue contours, 15.8 GHz), correspond to the bright Hα ribbons. Panels (b1), (b2), and (b3) depict the flare at its peak in BFI/TiO, AIA/193 Å, and VIS/Hα+0.8 Å images, respectively. The cyan and yellow contours indicate the footpoint and loop-top sources observed in EOVSA 17.5 GHz and 14.1 GHz channels. BFI/TiO data resolved three strong WL emission kernels (K1, K3, and K3 in panel (b1)). The red contours outline 5% enhancement of TiO quiet-Sun intensity. The K2r area in panel (a3) is selected to plot the EOVSA 14.9 GHz light curve. An animation for this figure presents this magnetic field emergence, filament eruption, and flare in EUV and Hα observations from 18:30 UT to 20:45 UT.

(An animation of this figure is available in the online article.)

shown in panel (a3) was selected for further analysis with EOVSA radio data. We further examine the data sets of these ROIs and report several novel findings with this event.

3.1. Emergence of Twisted Flux Rope and Formation/Eruption of Filament

The continuous emergence of the magnetic field dominated the evolution of AR 13110 during our observing period. As shown in Figure 2, the K2 area includes two small sunspots of different polarities. A slim and straight light bridge (LB) separates the two pores as a PIL. The gradual evolution of LB began with the appearance of two dark absorption features (cyan arrows). They showed up as delicate fibrils that eventually became prominent alternating bright–dark spiral structures. H. Wang et al. (2018) speculated that such structures are photospheric signatures of a twisted magnetic flux rope. V. Yurchyshyn et al. (2017) observed a similar LB transformation prior to an X1.6 flare with multiple small filament eruptions. In our study, the formation of a twisted chromospheric filament was also observed with VIS/Hα spectroscopic images. The time sequence of VIS/Hα images indicated that minor absorption fibrils arose from the K2 area. In the initial stage, they appeared as a parallel loop structure aligned with the PIL. As the emergence of the presumed twisted flux rope continued, the new rising loops interacted with these parallel loops. Eventually, a highly twisted filament formed above the magnetic flux emergence region during 90 minutes. Although the direction of the filament is somewhat sheared relative to the photospheric LB, some filament barbs appear to be parallel to and root in the LB.

The equilibrium of this system started to break up around 19:50 UT when prominent detwisting motions were witnessed in the Hα filament. The subsequent filament eruption process can be divided into three phases according to the ascending speed. As shown in the AIA 171 Å time–distance slices, the filament was slowly rising until 20:15 UT at an average speed of 12 km s^{-1}. From 19:55 UT to 20:14 UT, the projected height of the Hα filament (away from the PIL in the plane of the sky)

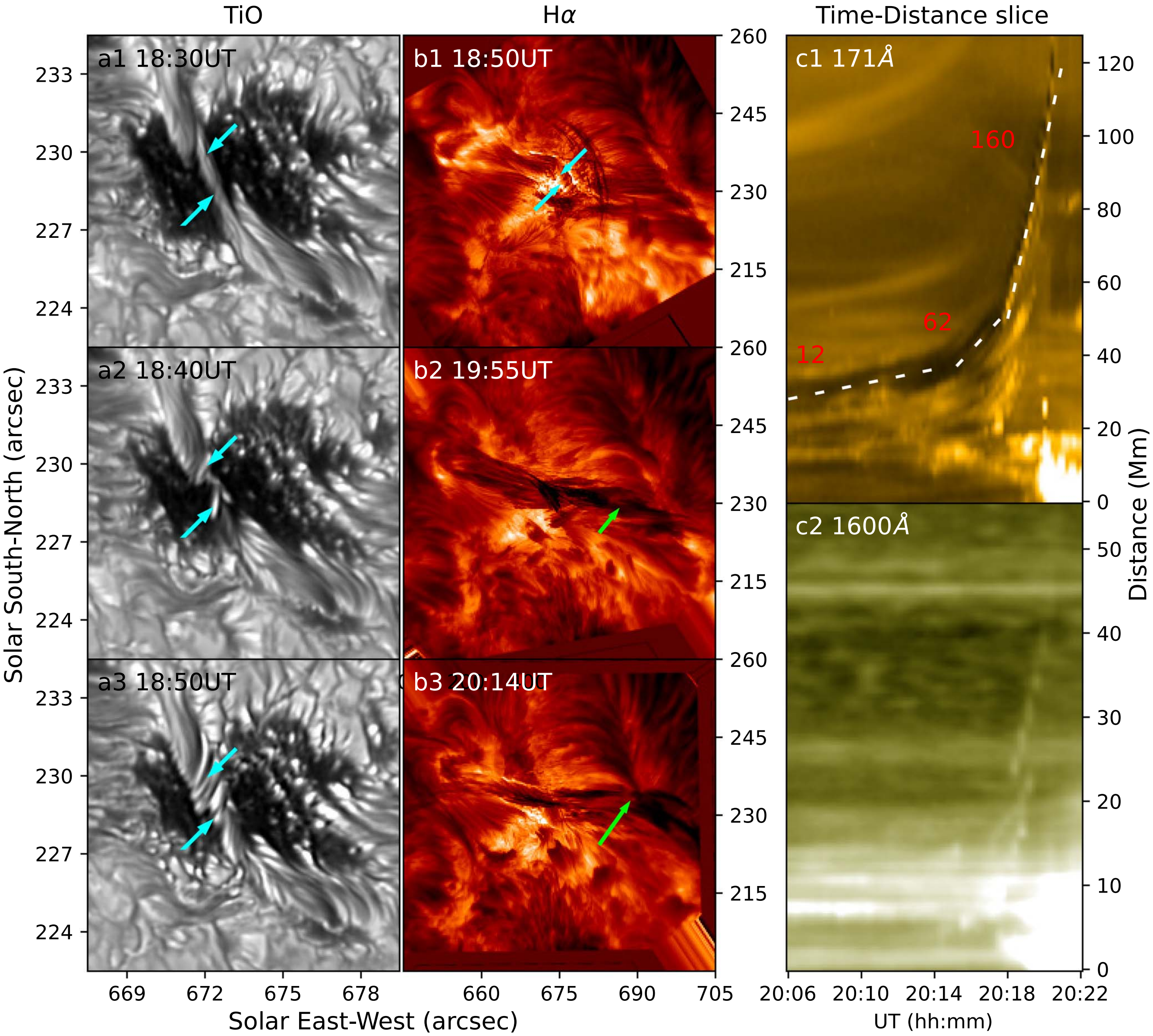

Figure 2. Filament eruption and its origin. Panels (a1), (a2), and (a3) are zoom-in photospheric images of the ROI K2. Cyan arrows indicate the emergence and development of twisted magnetic flux rope structure. Panels (b1), (b2), and (b3) present chromosphere observations in Hα line center in the GST full FOV. The cyan arrows in panel (b1) point to the same positions as of those in panels (a1)–(a3). Green arrows root in the PIL and point to the rising filament. Panels (c1) and (c2) are time–distance slices taken along yellow dashed line in Figure 1.

(An animation of this figure is available in the online article.)

increases from around 1500 to 3000 km as indicated by the green arrows in Figures 2(b2) and (b3). The filament was then accelerated; in the next five minutes, it rose at a speed of 62 km s^{-1} and then erupted with a speed above 160 km s^{-1}, accompanied by flare ribbons. Plasma was significantly heated in this event, as evidenced by the hot flare loops observed in the AIA 1600 Å channel. We note that there are multiple erupting components within the AIA 171 and 1600 Å time–distance slices, which can explain the double-peak structure of the HXR light curves in Figure 5.

3.2. Evolution of White-light Flare Ribbons

Between 20:20 UT and 20:23 UT, three WL flare ribbons were seen in HMI/I_c and BFI/TiO data as well as in the near-infrared NIRIS/Fe I 1.56 μm Stokes I image. Their intensities were significantly enhanced, making them noticeable in animated intensity and differential images (Figures 3 and 4). The enhanced brightening in these wavelengths suggests substantial heat deposits at different heights. The upper kernel K1 and lower kernel K3 exhibited clear separation motions, as expected from the two-ribbon flare model (CSHKP model; E. Priest & T. Forbes 2000). Such separating flare ribbons are typically seen in HXR, UV, or chromospheric spectral lines imaging (H. Wang et al. 2003; Y. Xu et al. 2022).

The WLF kernel, K1, appears along the upper left PIL and across a group of pores. Figure 3 provides a zoom-in view of the kernel in multiple wavelengths. The WL emission kernel slightly moves northward during the flare peak at 9 km s^{-1} apparent speed in the plane of the sky. Simultaneous observations in TiO

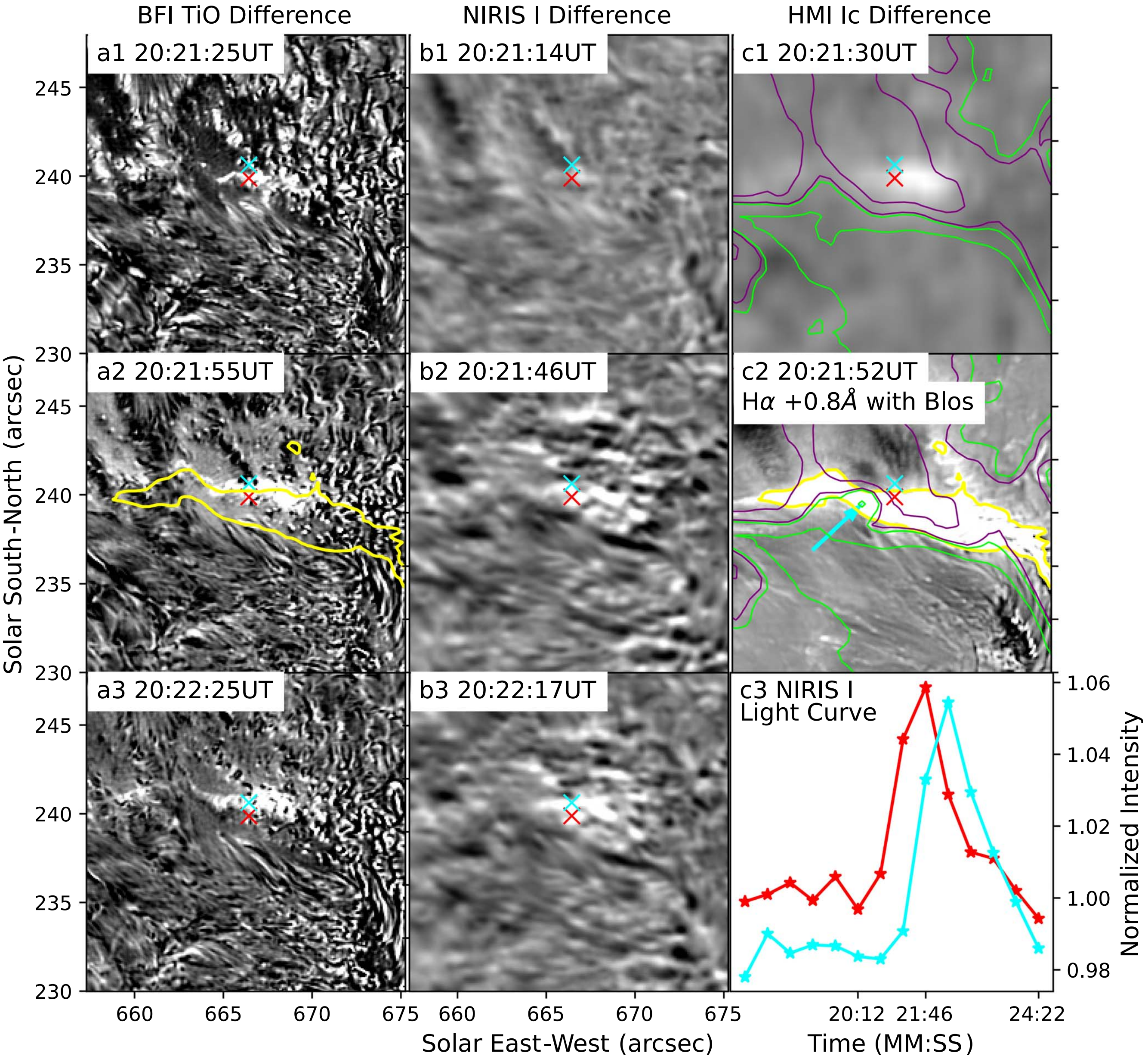

Figure 3. Zoom-in images at K1. Panels (a1)–(a3), (b1)–(b3), and (c1) present differential images of the upper WL ribbon at BFI/TiO 7057 Å, NIRIS/Fe I 1.56 μm and HMI/I_c, respectively. Panel (c2) is a Hα red-wing image, and yellow contours in panels (a2) and (c2) are plotted to illustrate the position of the Hα flare ribbon. Green and purple contours indicate the positive and negative polarities of the HMI LOS magnetic field. The LOS magnetic field in panels (c1) and (c2) are from before flare (20:18:30 UT) and during flare (20:21:30 UT), respectively. The cyan and red cross symbols mark positions of TiO WL kernel core at 20:21:25 UT and 20:22:25 UT. The IR light curves from NIRIS Stokes I at the two positions are plotted in panel (c3). An animation with BFI/TiO, HMI/I_c differential images and VIS/Hα, NIRIS/Fe I 1.56 μm intensity images is available to present the flare ribbon evolution during the flare peak period.

(An animation of this figure is available in the online article.)

and Hα +0.8 Å reveal that the WL emission kernel is located at the leading edge of the Hα flare ribbon. The magnetic field on the north side of the PIL is about –800 G.

The lower WLF kernel, K3, is situated in a unipolar region between AR 13110 satellite pores and the mean sunspot. As presented in Figure 4, the TiO WL kernels and Hα flare ribbons in this region exhibit greater extension in area and more noticeable migration in distance and speed. The TiO WL kernels are located along the front of the flare ribbons visible in simultaneous Hα red-wing observations. The WLF kernel progresses southeastward from AR 13110 north sunspots to the main sunspot, with an apparent velocity of 55 km s^{-1} and exceeds 8 Mm of total path. The strength of the local electric field, E_c, in the current sheet, can be derived in a simplified way from the observed horizontal velocity, v_t, and normal component of the magnetic field, B_n, as proposed by T. Forbes & J. Lin (2000):

$$E_c = v_t B_n. \tag{1}$$

Since the AR was not close to disk center ($\mu \equiv \cos\theta = 0.66$), we inspected the HMI vector magnetic field before the flare for its normal component and thus confirmed that the B_n in the K3 area was about 200 G. As the WLF ribbon K3 moved in the north–south direction and the AR was not far from the solar

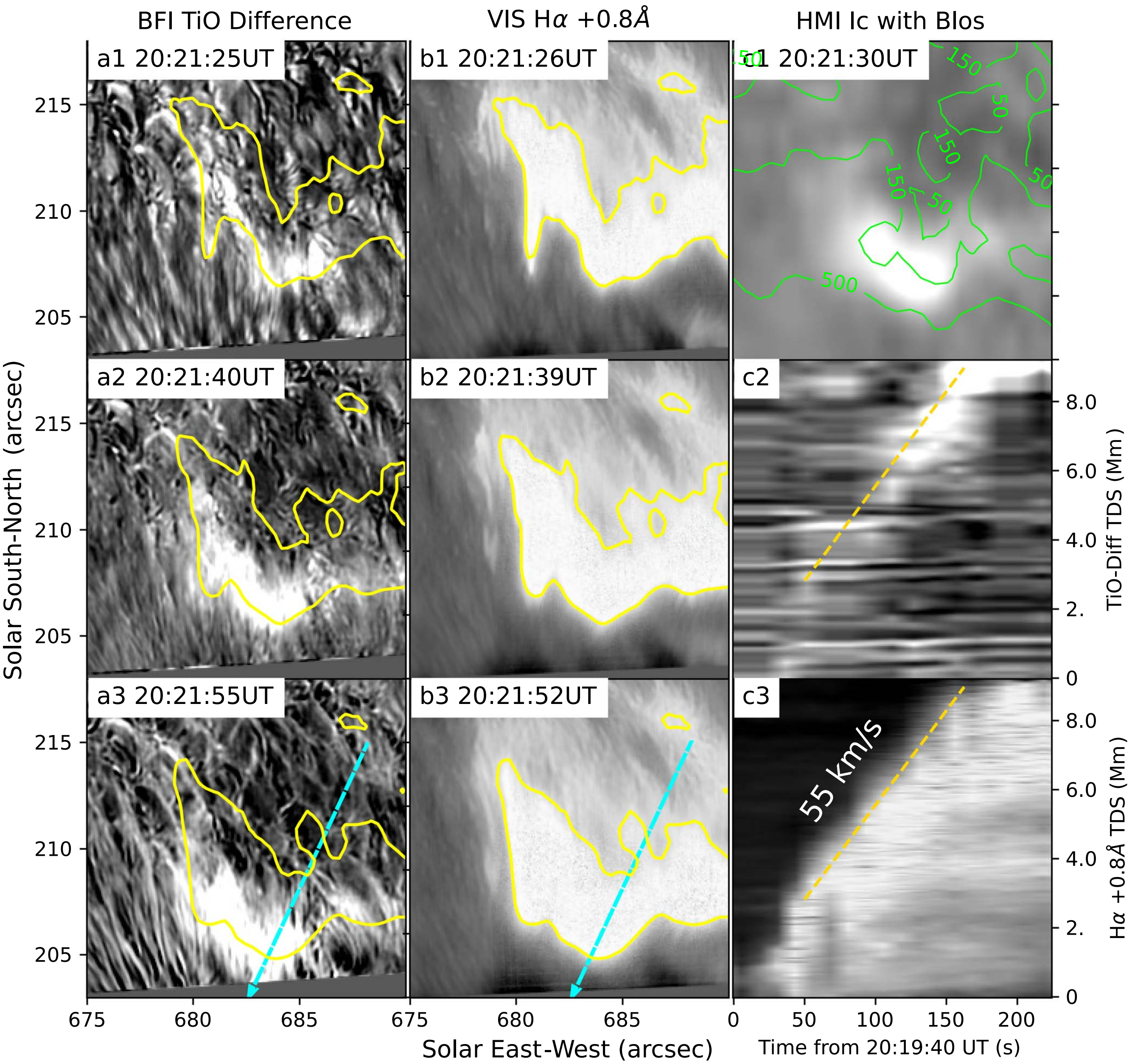

Figure 4. Zoom-in images at K3. Panels (a1)–(a3) and (c1) present the lower WLF ribbon resolved by BFI/TiO and HMI/I_c. Panels (b1)–(b3) displays flare ribbon in the chromosphere recorded by VIS/Hα red-wing images. Yellow contours in panels (a1)–(a3) and (b1)–(b3) indicate the leading edge of the Hα flare ribbon. Green contours in panel (c3) indicate the positive polarities of the LOS magnetic field. The cyan arrows in panels (a3) and (b3) indicate the spatial evolution of this flare ribbon. Panels (c2) and (c3) are TiO and Hα time–distance slices made along the cyan arrows.

equator, we may use the measured 55 km s^{-1} velocity as v_t. The average electric field, E_c, calculated at the WL kernel K3 was found to be about 11 V cm^{-1}, while the average electric field at the WL kernel K1 was approximately 10.6 V cm^{-1}. The local electric fields calculated for the two ribbons moving across opposite polarity fields are thus conserved.

The flare ribbon in the H$_\alpha$ red-wing images (panels (b1), (b2), and (b3)) contains a condensed leading edge and diffused tail. The TiO WL kernels in panels (a1)–(a3) correspond well to the simultaneous H$_\alpha$ flare ribbons in panels (b1)–(b3). The morphology of the TiO WL kernel and the leading edge of the Hα flare ribbon reveals the fine structure at the lower-atmosphere feet of flare loops and their evolution in the photospheric magnetic field distributions.

3.3. *Origin of White-light Emission*

The panels (a1)–(a3) and (b1)–(b3) of Figure 5 provide the flux of GBM/HXR versus various energy band light curves of BFI/TiO, HMI/I_c, and EOVSA/14.9 GHz, derived from different WL/radio kernels in panels (c1)–(c3). Notably, the HXR and radio data sets are obtained with exceptionally high time cadence, revealing intricate structures with fast-varying spikes in the light curves. Although the TiO observation is conducted at a longer cadence (15 s), the light curve of the enhanced emission in the continuum exhibits a remarkable temporal correlation with the HXR and microwave light curves. Nearly every minor spike in the HXR flux light curve is associated with a corresponding brightening in the TiO light curves. Specifically, after carefully inspecting the HXR light

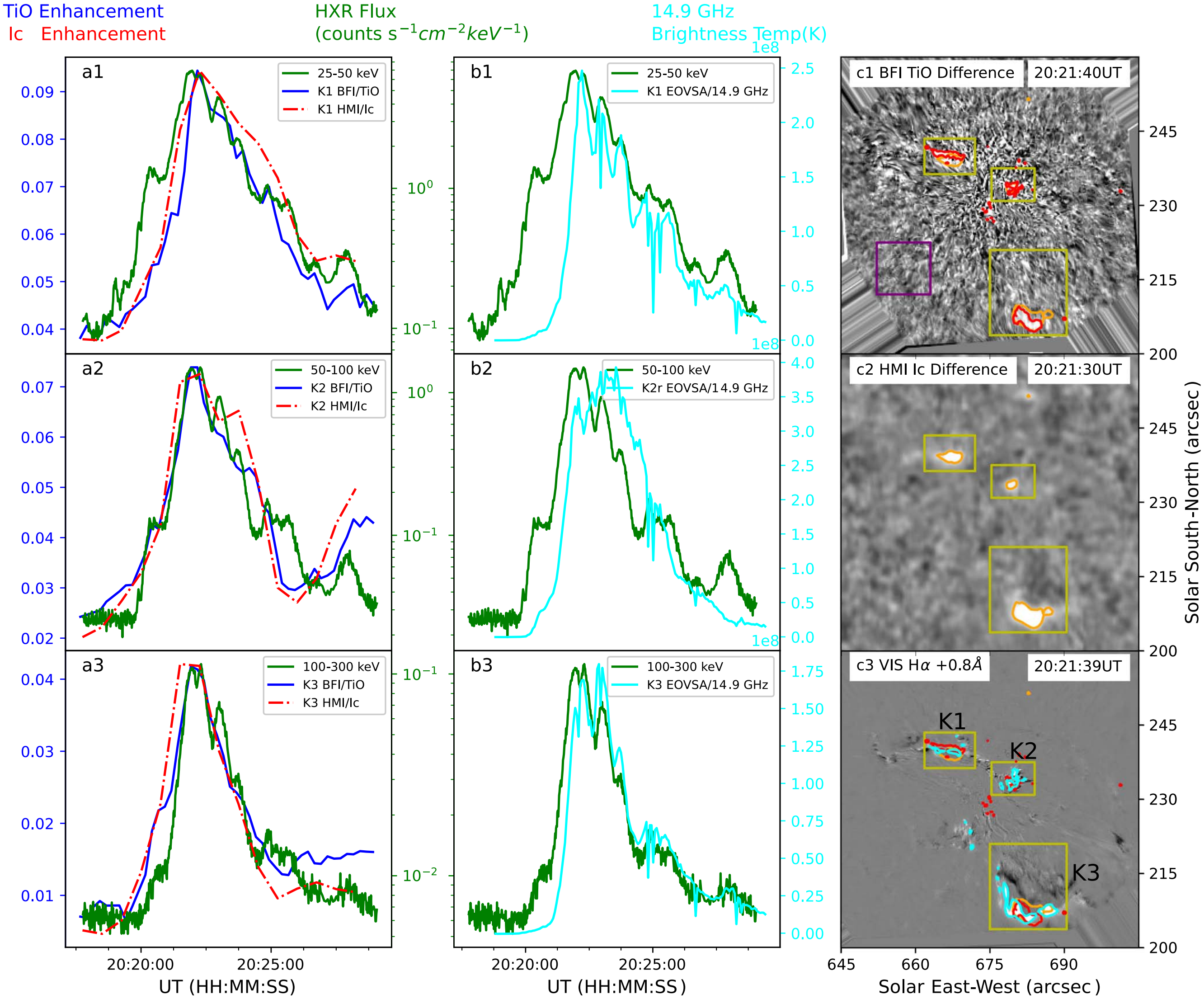

Figure 5. Multiwavelength flare light curves and flare ribbons. Panels (c1), (c2), and (c3) present a BFI/TiO running difference image, an HMI/I_c base difference image, and a VIS/Hα line center running difference image, respectively. Three WLF ribbons are indicated by the yellow rectangles. The red and orange contours indicate 5% enhancement in BFI/TiO and HMI/I_c. The cyan contours indicate 30% enhancement in VIS/Hα. Panels (a1)–(a3) present the correspondence between Fermi/HXR (green solid, multiple energy bands) and averaged WL intensity enhancements in BFI/TiO (blue solid) and HMI/I_c (red dotted–dashed) in the yellow areas. The background variation from a relatively quiet area (purple square in panel (c1)) has been subtracted in each wavelength. The HMI/I_c light curve is plotted in an adjusted anonymous scale to match the BFI/TiO amplitude. Panels (b1)–(b3) present the Fermi/HXR light curve in multiple energy bands and averaged EOVSA 14.9 GHz light curve (cyan solid) in each high-frequency radio source (K1, K2r, K3).

curve, we discover a double-peak structure during the flare maximum period (20:21:30–20:23:00 UT). The TiO light curve from K1 only responds to the second peak, while the TiO light curve from K2 and K3 corresponds to the first HXR peak. This discovery is confirmed by the high-cadence radio flux time profile in Figures 5(b1)–(b3). The tight temporal correlation between the TiO intensity and HXR flux time profiles strongly suggests that the enhanced WL emission in this event is associated with flare energetic particles.

We further estimate the total energy carried in nonthermal electrons through Fermi/HXR spectral analysis utilizing the OSPEX package in SSWIDL (R. Schwartz et al. 2002). The HXR spectrum has been fitted using a combination of isothermal emissions as the thermal component and thick-target bremsstrahlung model assuming the broken power-law distribution for the nonthermal component. The selected fitted time intervals range from 20:20:30 to 20:22:30 UT with 30 s steps. The energy flux can be estimated using the equation $\int_{E_c}^{E_{\max}} E \cdot F(E)dE$, where $F(E)$ is the electron flux spectra derived from the spectral fitting results. The low-energy cutoff, E_c, is fixed at 20 keV, and $E_{\max}$ is the high-energy cutoff fixed at 32,000 keV by default. The fitted break energy is 146.00 ± 6.30 keV, and the spectral index below (above) the break energy is 2.13 ± 0.12 (4.39 ± 0.03) at the peak time. The power of nonthermal electrons varies in the range of $\sim$5–8 $\times 10^{27}$ erg s^{-1}, with a value of $8.8 \pm 1.0 \times 10^{27}$ erg s^{-1} at the peak time 20:21:30–20:22:00 UT. Thus, the total energy carried in nonthermal electrons (>20 keV), integrated from 20:20:30 to 20:22:30 UT is $8.30 \pm 0.90 \times 10^{29}$ erg. The total area of the WL kernels with intensity enhancement greater than 10% over the quiet-Sun intensity, measured using the BFI/TiO difference image, was calculated as 4.24×10^{16} cm^2. Thus, the fluence (>20 keV) is $1.97 \pm 0.21 \times 10^{13}$ erg cm^{-2}. The energy flux density (>20 keV) in the peak time period is

$2.07 \pm 0.23 \times 10^{11}$ erg cm^{-2} s^{-1}. Given that energetic electrons at higher energies (>50 keV) exhibit close association with WL emission (M. Kuhar et al. 2016; V. Yurchyshyn et al. 2017), the fluence (>60 keV) is $7.20 \pm 1.00 \times 10^{12}$ erg cm^{-2}. The energy flux density (>60 keV) in the peak time period is $1.05 \pm 0.17 \times 10^{11}$ erg cm^{-2} s^{-1}.

4. Summary and Discussion

Based on multiwavelength observations provided by GST, EOVSA, SDO, and Fermi, we investigate the magnetic field evolution, filament eruption, and WLF emission mechanism for the X1.0 flare on 2024 October 2. We find the following results.

1. GST observed a strong emergence of a highly twisted magnetic flux rope in the photosphere prior to the formation of chromosphere filament. The Hα filament first appears along the PIL of the emerging flux and then orients under the influence of shear flows.
2. We inspected the separation motion of the WLF ribbons in the visible band with unprecedented high spatial and temporal resolutions. The average speed of the WL ribbon K1 is 9 km s^{-1} in a strong magnetic field (800 G) region inside the major sunspots, and K3 moves at a 55 km s^{-1} average speed in a weak magnetic field (150 G) region between the sunspots. Furthermore, observation with NIRIS Fe 1.56 μm spectropolarimetry images confirms the separation motions of the flare ribbon in the deep photosphere (D. Cabrera Solana et al. 2005).
3. Simultaneous high-cadence observations of HXR flux and TiO intensity exhibit close correlations in their time profiles, indicating that heating associated with high-energy electrons should be responsible for the compact and intense TiO WLF ribbon cores.

Y. Xu et al. (2004, 2006) reported separating flare ribbons seen in near-infrared observations. The IR ribbons in their X10 flare moved over weak field regions at a rate of 38 km s^{-1}, which decreased to about 19 km s^{-1} when the ribbons encountered stronger magnetic fields. R. A. Maurya & A. Ambastha (2009) observed WL ribbon motions in X17 and X10 flares observed by the global oscillation network group. These authors reported that the maximum velocity of a WLF ribbon in each event to be 45 ± 6 km s^{-1} and 33 ± 6 km s^{-1}, respectively. G. S. Kerr & L. Fletcher (2014) analyzed an X2.2 flare using Hinode/SOT broadband red, green, and blue continuum data. The WLF footpoints in this event moved slightly inside the umbra area of a rotating sunspot group with complicated structure. Taking advantage of GST, we report the moving WLF ribbons simultaneously in several wavelengths and accurately measure the moving speed for each WL ribbon. The northern WL kernel K1 moves in an area with a magnetic field of −800 G at a speed of 9 km s^{-1}, and the southern WL kernel K3 moves in an area with 150 G at a speed of 55 km s^{-1}. The average local electric field calculated from the two WLF ribbons was determined to be about 11 V cm^{-1}, which is in the middle of the range of values reported in previous studies (J. Qiu et al. 2002; H. Wang et al. 2003; M. D. Kazachenko et al. 2015). The WLF ribbon K3 was moving at the highest velocity and across the weakest magnetic fields among all reported in the past WLF studies. Meanwhile, the velocity difference and local magnetic field flux density difference between the two WLF ribbons are also larger than any event reported before. Previously observed WLF ribbons are reported inside the ARs and exist almost only on-site in the penumbrae or umbrae structures with much slower speed and shorter total distance.

As described in Figures 3(c1) and (c2), the WL kernel K1 moves northward from the PIL. The cyan arrow indicates an intrusion from positive to negative polarity in the HMI LOS magnetogram. This positive polarity magnetic intrusion develops and increases when the WL kernel sweeps northward, then decays and moves back when the WL emission disappears. At the arrowhead position, HMI/Blos changes from −800 to 600 G along with the WL kernel and recovers after the flare impulsive phase. Such temporary magnetic field changes associated with flares are reported as magnetic transients and are generally found near the flare loop footpoints. Magnetic transients and WLFs are closely related (B. J. Harker & A. A. Pevtsov 2013; Y. Song & H. Tian 2018). However, it could be an artifact of the data analysis algorithm (J. Qiu & D. Gary 2003; V. Yurchyshyn et al. 2004) or not (B. J. Harker & A. A. Pevtsov 2013). M. Švanda et al. (2018) also stressed that caution needs to be taken when interpreting increased intensity detected in HMI/I_c data during the flare period. Without inspecting the HMI line profile, it is not possible to know whether the derived HMI/I_c enhancement is from the continuum or it is from the disturbed spectral line shape.

The relationship between flare WL emission and flare energetic particles has been widely discussed. Previous high-resolution observations (Y. Xu et al. 2006; V. Yurchyshyn et al. 2017) resolved compact cores and extended halos in the WLF ribbons. The light curves on the cores present HXR-like impulsive profiles. The light curves of the halos, in contrast, show Hα or soft X-ray-like outlines. It is important to note that using a proton-beam-heating simulation grid (by G. S. Kerr et al. 2023), V. M. Sadykov et al. (2023) suggested that flare-accelerated proton beams can contribute to the enhancements of the continuum near the Fe I 6173 Å line as well. D. Li et al. (2023) studied a WLF at the limb and suggested that both the white-light enhancement and the chromospheric evaporation are triggered and driven by nonthermal electrons. D.-C. Song et al. (2023) analyzed the same X1.0 flare event with CHASE imaging spectrum data and observation-constrained radiative hydrodynamic simulations. Strong HXR emission up to 300 keV has been recorded for our flare event, revealing the nonthermal origin of the WL heating source. The authors synthesized line profiles (Fe I 6569 Å, Hα) with radiative hydrodynamic simulation and found that heating from a nonthermal electron beam together with its induced radiative backwarming is not enough to explain the WL enhancement with spectrum changes during the flare. Unfortunately, with their 45–70 s cadence WL data, it is difficult to resolve the rapid correspondence between flare HXR and WL emission. With high spatial- and temporal-resolution BFI/TiO data, we located the core of WL emission (10% brightening increase relative to the quiet Sun) in small but well-defined areas. The no-delay cotemporal high-cadence HXR, microwave, and WL emission profiles indicate direct heating by flare energetic particles. The energy flux density during the flare peak is $2.07 \pm 0.23 \times 10^{11}$ erg cm^{-2} s^{-1}, which provides a reference data point for future flare simulations.

The 15 s cadence TiO photosphere data in this study resolved the emergence of the twisted magnetic flux rope, separation motion of WLF ribbons, and no-delay correspondence between

HXR and WL emission. However, more details of the WLFs could be revealed with higher temporal resolution. Depending on this study and previous results (J. Qiu et al. 2002), the authors expect that a 1 s level or even a subsecond level resolution instrument will help scientists better understand the physics of WLFs.

Acknowledgments

The authors appreciate the use of data from the Goode Solar Telescope (GST) of the Big Bear Solar Observatory (BBSO). The operation of BBSO is supported by the US NSF AGS-2309939 grant and the New Jersey Institute of Technology (NJIT). GST operation is partly supported by the Korea Astronomy and Space Science Institute and the Seoul National University. The Expanded Owens Valley Solar Array (EOVSA) was designed and built and is now operated by NJIT as a community facility. EOVSA operations are supported by NSF grant AGS-2130832 to NJIT. X.Y., W.C., and V.Y. are supported by NSF grants AST-2108235, AGS-2401229, 2309939, 2408174, and 2300341. J.Q. is supported by NSF grants AST-2407849 and AGS-2401228.

Facilities: Big Bear Observatory (BFI, VIS, and NIRIS), OVRO:SA, SDO (AIA and HMI), Fermi (GBM).

ORCID iDs

Xu Yang https://orcid.org/0000-0002-3238-0779
Meiqi Wang https://orcid.org/0000-0002-2633-3562
Andrew Cao https://orcid.org/0009-0004-3700-4440
Kaifan Ji https://orcid.org/0000-0001-8950-3875
Vasyl Yurchyshyn https://orcid.org/0000-0001-9982-2175
Jiong Qiu https://orcid.org/0000-0002-2797-744X
Sijie Yu https://orcid.org/0000-0003-2872-2614
Jinhua Shen https://orcid.org/0000-0003-4439-4972
Wenda Cao https://orcid.org/0000-0003-2427-6047

References

Aboudarham, J., & Henoux, J. C. 1986, A&A, 168, 301
Ahn, K., Cao, W., Shumko, S., & Chae, J. 2016, AAS/SPD Meeting, 47, 2.07
Atwood, W. B., Abdo, A. A., Ackermann, M., et al. 2009, ApJ, 697, 1071
Berdyugina, S. V., Solanki, S. K., & Frutiger, C. 2003, A&A, 412, 513
Cabrera Solana, D., Bellot Rubio, L. R., & del Toro Iniesta, J. C. 2005, A&A, 439, 687
Cai, Y.-F., Yang, X., Xiang, Y.-Y., et al. 2022, RAA, 22, 065010
Cao, W., Goode, P. R., Ahn, K., et al. 2012, in ASP Conf. Ser. 463, Second ATST-EAST Meeting: Magnetic Fields from the Photosphere to the Corona, ed. T. R. Rimmele et al. (San Francisco, CA: ASP), 291
Cao, W., Gorceix, N., Coulter, R., Coulter, A., & Goode, P. R. 2010a, Proc. SPIE, 7733, 773330
Cao, W., Gorceix, N., Coulter, R., et al. 2010b, AN, 331, 636
Ding, M. D., Fang, C., & Yun, H. S. 1999, ApJ, 512, 454
Fletcher, L., & Hudson, H. S. 2008, ApJ, 675, 1645
Forbes, T., & Lin, J. 2000, JASTP, 62, 1499
Gan, W., Zhu, C., Deng, Y., et al. 2023, SoPh, 298, 68
Gan, W. Q., & Mauas, P. J. D. 1994, ApJ, 430, 891
Gary, D. E., Chen, B., Dennis, B. R., et al. 2018, ApJ, 863, 83
Goode, P. R., & Cao, W. 2012, Proc. SPIE, 8444, 844403
Hao, Q., Guo, Y., Dai, Y., et al. 2012, A&A, 544, L17
Harker, B. J., & Pevtsov, A. A. 2013, ApJ, 778, 175
Heinzel, P., & Kleint, L. 2014, ApJL, 794, L23
Huang, N.-Y., Xu, Y., & Wang, H. 2016, RAA, 16, 177
Hudson, H. S. 1972, SoPh, 24, 414
Hudson, H. S., Acton, L. W., Hirayama, T., & Uchida, Y. 1992, PASJ, 44, L77
Jess, D. B., Mathioudakis, M., Crockett, P. J., & Keenan, F. P. 2008, ApJL, 688, L119
Jing, Z., Li, Y., Feng, L., et al. 2024, SoPh, 299, 11
Kazachenko, M. D., Fisher, G. H., Welsch, B. T., Liu, Y., & Sun, X. 2015, ApJ, 811, 16
Kerr, G. S., Allred, J. C., Kowalski, A. F., et al. 2023, ApJ, 945, 118
Kerr, G. S., & Fletcher, L. 2014, ApJ, 783, 98
Kowalski, A. F., Hawley, S. L., Carlsson, M., et al. 2015, SoPh, 290, 3487
Kuhar, M., Krucker, S., Oliveros, J. C. M., et al. 2016, ApJ, 816, 6
Lemen, J. R., Title, A. M., Akin, D. J., et al. 2011, SoPh, 275, 17
Li, C., Fang, C., Li, Z., et al. 2022, SCPMA, 65, 289602
Li, D., Li, C., Qiu, Y., et al. 2023, ApJ, 954, 7
Li, Y., Jing, Z., Song, D.-C., et al. 2024, ApJL, 963, L3
Machado, M. E., Emslie, A. G., & Avrett, E. H. 1989, SoPh, 124, 303
Matthews, S. A., van Driel-Gesztelyi, L., Hudson, H. S., & Nitta, N. V. 2003, A&A, 409, 1107
Maurya, R. A., & Ambastha, A. 2009, SoPh, 258, 31
Meegan, C., Lichti, G., Bhat, P. N., et al. 2009, ApJ, 702, 791
Metcalf, T. R., Alexander, D., Hudson, H. S., & Longcope, D. W. 2003, ApJ, 595, 483
Metcalf, T. R., Canfield, R. C., Avrett, E. H., & Metcalf, F. T. 1990, ApJ, 350, 463
Neidig, D. 1989, SoPh, 121, 261
Priest, E., & Forbes, T. 2000, Magnetic Reconnection: MHD Theory and Applications (Cambridge: Cambridge Univ. Press)
Procházka, O., Reid, A., Milligan, R. O., et al. 2018, ApJ, 862, 76
Qiu, J., & Gary, D. 2003, ApJ, 599, 615
Qiu, J., Lee, J., Gary, D. E., & Wang, H. 2002, ApJ, 565, 1335
Sadykov, V. M., Stefan, J. T., Kosovichev, A. G., et al. 2023, ApJ, 960, 80
Scherrer, P. H., Schou, J., Bush, R. I., et al. 2011, SoPh, 275, 207
Schou, J., Scherrer, P. H., Bush, R. I., et al. 2011, SoPh, 275, 229
Schwartz, R., Csillaghy, A., Tolbert, A., et al. 2002, SoPh, 210, 165
Song, D.-C., Tian, J., Li, Y., et al. 2023, ApJL, 952, L6
Song, Y., & Tian, H. 2018, ApJ, 867, 159
Song, Y., Tian, H., Zhu, X., et al. 2020, ApJL, 893, L13
Suematsu, Y., Tsuneta, S., Ichimoto, K., et al. 2008, SoPh, 249, 197
Švanda, M., Jurck, J., Kaparov, J., & Kleint, L. 2018, ApJ, 860, 144
Wang, H., Qiu, J., Jing, J., & Zhang, H. 2003, ApJ, 593, 564
Wang, H., Yurchyshyn, V., Liu, C., et al. 2018, RNAAS, 2, 8
Watanabe, K., Kitagawa, J., & Masuda, S. 2017, ApJ, 850, 204
Wöger, F., & von der Lühe, O. 2007, ApOpt, 46, 8015
Xu, Y., Cao, W., Liu, C., et al. 2004, ApJL, 607, L131
Xu, Y., Cao, W., Liu, C., et al. 2006, ApJ, 641, 1210
Xu, Y., Yang, X., Kerr, G. S., et al. 2022, ApJL, 924, L18
Yang, X., Cao, W., & Yurchyshyn, V. 2022, ApJS, 262, 55
Yurchyshyn, V., Kumar, P., Abramenko, V., et al. 2017, ApJ, 838, 32
Yurchyshyn, V., Wang, H., Abramenko, V., Spirock, T. J., & Krucker, S. 2004, ApJ, 605, 546